The Intraseasonal Atmospheric Angular Momentum Associated with MJO Convective Initiations

Naoko Sakaeda[1] and Paul E. Roundy[2]

[1]Physical Sciences Division, NOAA/Earth System Research Laboratory

Boulder, Colorado, USA

[2]Dept. Atmospheric and Environmental Science

University at Albany, State University of New York, USA

***Corresponding Author address**

Naoko Sakaeda

NOAA Earth System Research Laboratory

Physical Sciences Division

325 Broadway, Boulder, Colorado 80305

Email: naoko.sakaeda@noaa.gov

This is the author manuscript accepted for publication and has undergone full peer review but has not been through the copyediting, typesetting, pagination and proofreading process, which may lead to differences between this version and the Version of Record. Please cite this article as doi: 10.1002/qj.2740

Abstract

The first part of this study examines the driving mechanisms of the equatorial intraseasonal relative atmospheric angular momentum (AAM) and its dynamical relationship to the upper-tropospheric zonal wind over the Western Hemisphere (WH) during the convective initiation of the MJO over the Indian Ocean. The budget analysis shows that the main driver of the equatorial intraseasonal AAM anomaly is the meridional transport of momentum induced by the modulation of the background subtropical eddies by the intraseasonal eddies. While the subtropical eddies over the central Pacific basin partly drive the equatorial AAM by meridionally transporting the momentum, the equatorial zonal wind associated with the same subtropical eddies is zonally advected and locally amplified over the east Pacific and Atlantic basins. The common source phenomena that transport momentum results in simultaneous evolution of the WH upper-tropospheric zonal wind and the AAM on intraseasonal timescales, but their main driving mechanisms are different.

The second part of the study investigates the influence of the equatorial intraseasonal AAM state on the subsequent development of initiating MJO convection over the Indian Ocean. In the presence of the WH upper-tropospheric easterly wind, MJO convection tends to develop a stronger enhanced convective envelope when the initiation occurs during the negative intraseasonal AAM state, which strengthens and extends the upper-tropospheric easterly wind in the WH. When the AAM anomaly is positive, it tends to induce stronger mid-tropospheric convergence above the region of convective initiation, thereby suppressing the lower-tropospheric updraft and suppressing the further growth of convection. The results show that the

combined effects of the WH circumnavigating circulation and the AAM can influence the subsequent development of MJO convection over the Indian Ocean.

Key words: Madden-Julian oscillation; atmospheric angular momentum; momentum budget; intraseasonal convective initiation

Running Head: Atmospheric Angular Momentum and MJO Convective Initiation

1. Introduction

The evolution of the Madden-Julian Oscillation (MJO: Zhang, 2005) is often associated with particular patterns in the intraseasonal global atmospheric angular momentum (AAM) anomaly (Weickmann *et al*., 1992; Madden and Speth, 1995; Anderson and Rosen, 1983; Feldstein and Lee, 1995). The globally integrated AAM exchanges with the solid earth to conserve the total angular momentum of the earth and atmosphere, therefore the intraseasonal variability in the AAM is also associated with slight changes in the length-of-day (Madden, 1987; Dickey *et al*., 1991; Guzler and Ponte, 1990; Magana, 1993). The variability in the global relative AAM is associated with changes in the Hadley circulation, modulating the strength of zonal-mean overturning circulations in the tropics and subtropics (Kang and Lau, 1994; Weickmann *et al*., 1997). The intraseasonal globally integrated AAM anomaly evolves with intraseasonal zonally integrated AAM anomalies that initiate in the tropics and propagate poleward into both the Northern and Southern Hemispheres (Weickmann *et al*., 1997). The peak in the intraseasonal globally integrated AAM anomaly often occurs when the positive zonal AAM anomaly reaches the subtropics and when MJO convection is enhanced over the Pacific basin and suppressed over the Indian Ocean (Weickmann *et al.,* 1992; Feldstein and Lee, 1995; Weickmann and Sardeshmukh, 1994). Previous studies showed that the mountain and surface friction torques contribute to the evolution of the intraseasonal globally integrated AAM anomaly, while AAM flux convergence meridionally distributes the zonal-mean relative AAM anomaly (Weickmann and Sardemukh, 1994; Weickmann *et al.,* 1997). The intraseasonal mountain and surface friction torques as well as the flux convergence are often driven by

intraseasonal circulation associated with MJO convection in the tropics and extratropics (Feldstein and Lee, 1995; Madden, 1988; Weickmann *et al.,* 1997).

MJO convection is often associated with circulation patterns that are roughly similar to the response to a stationary tropical heat source, as found by Gill (1980), that has a Kelvin wave response to its east and a pair of Rossby gyres on its west (e.g., Kiladis *et al.,* 2005; Zhang, 2005) except that the MJO response also often includes a pair of opposite-signed Rossby gyres east of the convection. The tropical Rossby and Kelvin wave circulations that are associated with MJO convection propagate in the tropics and subtropics where they interact with major topography (e.g., the Andes Mountains, the Tibetan Plateau, and the Rocky Mountains), inducing anomalous mountain and friction torques (Weickmann and Sardeshmukh, 1994; Weickmann *et al.,* 1997; Feldstein and Lee, 1995). The intraseasonal AAM flux convergence results mostly from the modulation of the background eddies by intraseasonal eddy circulations (Weickmann *et al.,* 1997), where the background is defined as the seasonal or climatological time-mean state. In addition, the modulation of the background circulation by the intraseasonal subtropical Rossby gyres influences the strength and location of the subtropical jets, resulting in changes in the characteristics of synoptic scale midlatitude circulation such as Rossby wave breaking (MacRitchie and Roundy, 2015; Moore *et al*., 2010). The resultant changes in the midlatitude synoptic circulation such as Rossby wave breaking events can then feed back onto the intraseasonal circulation thereby contributing to the poleward propagation of the intraseasonal zonal-mean zonal wind (Lee *et al.*, 2007; Sakaeda and Roundy, 2014).

An intraseasonal globally-integrated AAM anomaly can also develop independently from the MJO (Marcus *et al.,* 1996; Dickey *et al.,* 1991; Weickmann and Berry, 2009) through the interactions of midlatitude synoptic waves with topography, which induce momentum exchange with the solid earth and transport momentum (e.g., Weickmann, 2003). However, the intraseasonal AAM anomaly in the tropics is strongly associated with the MJO. Variability in zonally and vertically integrated AAM in the tropics is dominated by the upper-tropospheric zonal wind (Kang and Lau, 1994; Weickmann *et al.,* 1997; Anderson and Rose, 1983). Previous studies focused on the evolution of the globally integrated intraseasonal AAM anomaly and its association with the MJO, yet these authors provided little emphasis on the driving mechanisms of the tropical zonal-mean intraseasonal AAM anomaly and dynamical association between the tropical AAM and MJO convection. Weickmann *et al.* (1997) and Sakaeda and Roundy (2014) found that the main driver for upper-tropospheric zonal-mean intraseasonal zonal wind is the meridional flux convergence that results from the strengthening or weakening of background eddies by intraseasonal winds. However, it is unclear whether this process dominates the development of zonal-mean intraseasonal AAM by generating large local or regional signals near a particular longitude or whether the momentum appears uniformly across all global longitudes. The difference would be important to understand the source of variability in the intraseasonal AAM anomaly in the tropics. The zonal-mean intraseasonal AAM typically propagates poleward from the tropics (e.g., Weickmann *et al.,* 1997), but local zonal momentum anomalies in the tropics can be generated by the equatorward transport of momentum from higher latitudes. Therefore, the association between the zonally symmetric and asymmetric circulations needs to

be further analyzed to understand the dynamical feedback mechanisms between the MJO and the extratropical circulation.

The background zonal wind associated with the seasonal cycle is westerly during northern winter in the upper-troposphere over the Western Hemisphere (WH), which enhances the equatorward propagation of midlatitude wave trains (Webster and Holton, 1982; Hoskin and Ambrizzi, 1993). Weickmann *et al.* (1992) suggested that the in-situ (i.e. not part of the circumnavigating signal) development of upper-tropospheric intraseasonal zonal wind anomalies over the WH occurs during the developing phase of the intraseasonal global AAM anomaly. Their results suggest that the development of the upper-tropospheric intraseasonal zonal wind anomalies over the WH is associated with momentum flux from the midlatitudes, and that this flux contributes to the evolution of zonal and global intraseasonal AAM anomaly. The intraseasonal zonal wind anomaly over the WH associated with the MJO was traditionally thought as a "free" or dry Kelvin wave radiated by MJO convection over the warm pool (e.g., Milliff and Madden, 1996; Salby *et al*., 1994). However, Sakaeda and Roundy (2015a) showed that a theoretical dry Kelvin wave cannot completely explain the structure or the driving mechanism of the upper-tropospheric intraseasonal zonal wind over the WH. They suggested that the initial development of the intraseasonal zonal wind over these basins is strongly coupled to the midlatitude circulation, and that the resultant wind signal is amplified as it advects background zonal wind in a region of background wind convergence over the east Pacific and Atlantic basins (consistent with Webster and Chang, 1988). Sakaeda and Roundy (2015b) further showed that as these wind anomalies propagate from the east Pacific into the Atlantic basin, they

begin to form a Kelvin wave structure, suggesting that the structure and dynamics of the intraseasonal circumnavigating signal change as it propagates through the WH.

Furthermore, Roundy (2014) showed that the sign of this upper-tropospheric intraseasonal zonal wind anomaly over the WH during the convective initiation of the MJO over the Indian Ocean is a significant marker of the likelihood of the subsequent amplitude of MJO convection becoming large (see also Sakaeda and Roundy, 2015a). The initiating MJO convection develops into a stronger and better-organized envelope following the easterly upper-tropospheric wind over the WH compared to the ones following the westerly wind anomaly over the same region. In addition, the upper-tropospheric zonal wind anomaly over the WH during the convective initiation of the MJO tends to be in phase with the zonal-mean intraseasonal AAM anomaly in the tropics (Sakaeda and Roundy, 2015a), suggesting that stronger MJO convection tends to develop during negative equatorial intraseasonal AAM anomalies, and the upper-tropospheric zonal wind anomalies in the WH may be the primary drivers of the equatorial intraseasonal AAM anomalies. However, MJO convection over the warm pool also induces a lower-tropospheric Kelvin wave circulation that propagates eastward across the globe (e.g., Salby and Hendon, 1994; Matthews, 2008; Matthews, 2000), which can interact with the Andes Mountains, where it induces mountain torques that project their signals onto AAM (Weickmann *et al.,* 1997). Therefore the association between the upper-tropospheric zonal wind over the WH and AAM in the tropics might be indirectly associated through surface torques. These previous studies motivate further investigation of the dynamical relationship between the upper-tropospheric zonal wind anomaly and the tropical zonal-mean AAM anomaly and potential impact of the

tropical AAM on the development of MJO convection. A number of studies have demonstrated the association between the MJO and the AAM, yet the impact of the AAM on the MJO has not been examined.

This study investigates dynamical links between intraseasonal upper-tropospheric zonal wind anomaly over the WH and tropical zonally integrated AAM anomaly using AAM budget analysis. The main questions addressed in this study are 1) What are the dynamical links between the upper-tropospheric intraseasonal zonal wind and zonally integrated AAM anomaly in the tropics and 2) What are the impacts of the AAM anomaly, if any, on MJO convection?

2. Data and Methods

This study uses the NCEP Climate Forecast System Reanalysis (CFSR: Saha *et al.,* 2010) with 2.5° horizontal resolution and 37 isobaric surfaces to calculate relative AAM and its budget terms. Tropical convection is represented by daily-interpolated outgoing longwave radiation data (OLR: Liebmann and Smith, 1996). The analyzed period of the study is December-January-February (DJF) from 1979 to 2010. The same MJO index as Sakaeda and Roundy (2015a, b) is used to estimate the state and strength of MJO convection. This MJO index is derived using the two leading modes of intraseasonal OLR anomaly extracted by empirical orthogonal function (EOF) analysis following the same method as Wheeler and Hendon (2004) except using the intraseasonal OLR anomaly only. The intraseasonal timescale is defined to have periods from 20

days to 100 days. All filtering in this study is done by applying the Fourier transform and inverting the transform after setting the Fourier coefficients outside a target frequency band to zero, following the technique of Wheeler and Kiladis (1999).

2.1. AAM Budget

The atmospheric angular momentum has its earth and relative components, but this study focuses on the relative component, m_r, which represents the atmospheric zonal wind (1):

$$m_r = ua\cos\phi \qquad (1)$$

where a is the radius of the earth and ϕ is latitude.

The zonally and vertically integrated quantity of m_r is referred to as M_r, and its budget equation is shown in (2).

$$\frac{\partial M_r}{\partial t} = \frac{\partial}{\partial t}\left[\{m_r\}\right] = -\left[\{\nabla\cdot(\mathbf{v}m_r)\}\right] + fa\cos\phi\left[\{v\}\right] - \frac{1}{g}\left[p_s\left(\frac{\partial z_s}{\partial\lambda}\right)\right] + a\cos\phi\left[\ddot{A}_s\right] \qquad (2)$$

$$\left[\{A\}\right] = a^2\cos\phi\int_0^{2\pi}\frac{1}{g}\int_0^{p_s} A\,dp\,d\lambda \qquad (3)$$

The right hand side (rhs) of (2) shows main dynamical terms that drive M_r, which are transport, Coriolis torque, mountain torque, and surface friction torque, in order from left to right. The curly and square brackets represent the vertical and zonal integrals, respectively, in (3). The limits of the vertical integral are from surface pressure to 1-hPa, which is the smallest pressure level available from the CFSR. In (2) and (3), $\mathbf{v} = (v, \dot{p})$ represents the meridional and vertical components of wind on isobaric surfaces, f the Coriolis parameter, g the acceleration due to

gravity, λ longitude, p pressure, z surface height, and $\ddot{A}_s$ the surface flux of zonal momentum. The subscript s indicates a variable at the surface of the earth. More detailed descriptions of the derivation of AAM budget terms are presented by Weickmann and Sardeshmukh (1994). To be precise, because the terms in (2) are integrated from the surface of the earth, the zonal flux convergence term ($\left[-\partial(um_r)/\partial x\right]$) is not zero near the surface of the earth where topography interferes with isobaric surfaces. However, the budget closes fairly well without the term and the inclusion of the term does not eliminate the residual (see section 3.2).

Similar to Sakaeda and Roundy (2014), temporal and zonal decomposition is applied to the transport term of (2) to examine the role of scale interactions. Both the wind and m_r are decomposed into zonal-mean and eddy (zonally asymmetric) components as shown in (4)

$$\mathbf{v} = [\mathbf{v}]/2\grave{A} + <\mathbf{v}> \qquad (4)$$

where the angle bracket indicates the eddy component. This zonal decomposition results in the transport term of (2) expanding into two terms as shown in (5)

$$-\left[\{\nabla\cdot(\mathbf{v}m_r)\}\right] = -\{[\mathbf{v}]\cdot\nabla[m_r]\} - \{\nabla\cdot[<\mathbf{v}><m_r>]\} \qquad (5)$$

where the first term represents the advection by zonal-mean circulation and the second term represents the flux convergence by eddies.

Each zonal-mean and eddy component is further decomposed into three timescales as shown in (6) and (7),

$$[\mathbf{v}] = [\overline{\mathbf{v}}] + [\mathbf{v}^*] + [\mathbf{v}'] \qquad (6)$$

$$<\mathbf{v}> = <\overline{\mathbf{v}}> + <\mathbf{v}^*> + <\mathbf{v}'> \qquad (7)$$

where the overbar indicates background state, the asterisk indicates intraseasonal timescales, and the prime indicates transient timescales. The intraseasonal timescales include periods of 20-100 days. Periods longer and shorter than the intraseasonal timescales are referred to as the background and transient timescales. The decomposition as shown in (4)-(7) expands each rhs term of (5) into 9 terms (not shown). When only the terms that are relevant to the intraseasonal tropical AAM anomaly are considered and terms with negligible scales in the tropics are discarded, the advection terms can be simplified as (8) and (9). The asterisk outside a bracket indicates the intraseasonal timescale part of the term inside that bracket.

$$-\{[\mathbf{v}]\cdot\nabla[m_r]\}^* \approx -\{[\overline{\mathbf{v}}]\cdot\nabla[m_r{}^*]\} - \{[\mathbf{v}^*]\cdot\nabla[\overline{m}_r]\} \quad (8)$$

$$-\{\nabla\cdot[<\mathbf{v}><m_r>]\}^* \approx -\{\nabla\cdot[<\overline{\mathbf{v}}><m_r{}^*>]\} - \{\nabla\cdot[<\mathbf{v}^*><\overline{m}_r>]\} \quad (9)$$

Consistent with previous studies (Weickmann *et al.,* 1997; Sakaeda and Roundy, 2014), scale analysis indicates that the advection term of zonal-mean momentum in the tropics is dominated by terms that result from interactions between background and intraseasonal winds (not shown).

2.2. Composite Analysis

The intraseasonal AAM anomaly and its budget terms are composited on the same sets of MJO convective initiation events as Sakaeda and Roundy (2015a, b). Sakaeda and Roundy (2015a, b) first identified initiating MJO convective events as days when the MJO index is in phase 1 and its amplitude is greater than or equal to 0.5. The center date of each of the identified MJO convective event is defined as day 0. Then, the MJO events are stratified into two sets of events based on whether 200-hPa intraseasonal zonal wind anomaly over the WH (2.5ºN-2.5ºS,

140ºW-40ºW) is easterly or westerly. The two sets of MJO convective events are referred to as easterly wind events and westerly wind events, and the study period includes 45 easterly wind events and 19 westerly wind events. By this definition, both the easterly and westerly wind events have initiating MJO convection over the Indian basin around day 0, yet one has easterly and the other has westerly 200-hPa intraseasonal zonal wind anomaly over the WH on day 0. The AAM budget terms and other fields are composited with time lags from day 0 of the easterly and westerly wind events. Positive and negative lags indicate days following and preceding day 0. The composites based on the easterly and westerly wind events allow us to compare the evolution of the equatorial AAM anomalies during those events in order to examine the association between the upper-tropospheric zonal wind and AAM anomalies during the convective initiation of the MJO. A Student's t-test assesses whether composited anomalies are statistically significantly different from zero with the number of degrees of freedom equal to the number of events. The difference between the two sets of events is calculated by subtracting composite means of westerly wind events from the ones of easterly wind events. The statistical significance of the composite difference between the easterly and westerly wind events is tested using two-sample Student's t-test. The AAM tendency is presented in the unit of Hadley (10^{18} kg m^2 s^{-2}).

3. Results

The first part of this section presents the results of the budget analysis on the intraseasonal equatorial AAM anomaly and its association with the upper-tropospheric zonal wind anomaly over the WH in section 3.1 and 3.2. Then, section 3.3 examines the potential role of the intraseasonal AAM state on the subsequent development of MJO convection over the Indian Ocean.

3.1. The Intraseasonal Upper-Tropospheric Zonal Wind and AAM Anomaly

Figure 1 shows 200-hPa intraseasonal zonal wind anomalies and zonally and vertically integrated relative AAM (M_r) averaged from 10°S to 5°N. The latitude band is centered slightly south of the equator since the intraseasonal AAM anomaly initiates there (e.g., Weickmann *et al.,* 1997). By construction, the easterly wind events have 200-hPa easterly wind anomaly and the westerly wind events have westerly wind anomaly over the WH on day 0 (Fig. 1a, b). As shown by Sakaeda and Roundy (2015a), 200-hPa zonal wind anomalies over the Eastern Hemisphere are mostly not significantly different prior to day 0 between the easterly and westerly wind events, but significant differences are apparent over the WH (Fig. 1c). During both the easterly and westerly events, the intraseasonal M_r anomaly tends to be in phase with 200-hPa intraseasonal zonal wind anomaly over the WH as shown in previous studies (e.g., Weickmann *et al.,* 1992). For example, the negative M_r anomaly in the easterly wind events peaks around day +8, when the 200-hPa intraseasonal easterly wind also peaks in the WH. The difference in the M_r anomaly between the easterly and westerly wind events also coincides with the difference in the 200-hPa zonal wind anomaly over the WH (Fig. 1c). The strong association between the

upper-tropospheric zonal wind over the WH and the M_r may suggest that the upper-tropospheric zonal wind over the WH dominates the evolution of equatorial M_r.

At the surface of the earth, a similar phase lag between the pressure anomalies (Fig. 2) and zonal wind anomalies (not shown) exists in the WH, suggesting that the surface friction torque and the mountain torque may also be important to the different evolutions of M_r between the easterly and westerly wind events. Figure 2 shows that during the easterly and westerly wind events, a positive surface pressure anomaly propagates with the suppressed convection over the Indian and western Pacific basins, but the pressure anomaly decouples from the convection and propagates more quickly across the central and eastern Pacific basins. This decoupling of the surface pressure anomaly from MJO convection has been observed in previous studies (e.g., Matthews, 2000; Sobel and Kim, 2012). However, during the westerly wind events, the surface pressure and OLR anomalies stay coupled farther east, resulting in the delayed arrival of the positive surface pressure anomaly to the Andes Mountains around 90°W. Likewise, the upper-tropospheric easterly wind anomaly on the east side of the suppressed convection also seems to stay coupled with the convection to its east during the westerly wind events, delaying the arrival of the upper-tropospheric easterly wind anomaly to the east Pacific basin (Fig. 1b). The positive surface pressure anomaly tends to lead the arrival of 200-hPa easterly wind anomaly in quadrature over the east Pacific basin. When the positive surface pressure anomaly arrives on the west side of the Andes Mountains, it induces a negative mountain torque on the atmosphere, thereby decreasing the M_r anomaly. Figures 1 and 2 show that the surface and 200-hPa circulation associated with the MJO tend to decouple from the convection over the same

longitude and propagate at a similar phase speed over the Pacific basins, suggesting that both the lower- and upper-tropospheric circulation over the WH are associated with the difference in the M_r anomaly between the easterly and westerly wind events.

As shown in previous studies (e.g., Weickmann and Sardeshmukh, 1994; Weickmann *et al.,* 1997), Fig. 3 shows that the intraseasonal M_r anomalies in the tropics propagate poleward in both the easterly and westerly wind events. Therefore the delay in the development of the intraseasonal AAM anomaly in the tropics between the easterly and westerly wind events results in both the delay of its poleward propagation and the subsequent time local maxima and minima of globally integrated intraseasonal AAM anomaly. The difference of the global distribution of AAM anomaly between the two sets of events shows a clear phase lag in time (Fig. 3c). By construction, both the easterly and westerly wind events have a similar geographical pattern of MJO convection (Fig. 2). However, the global distribution of AAM anomaly shows significant lags in Fig. 3, suggesting that the global intraseasonal AAM anomalies can be sensitive to slight differences in MJO convection or they can be driven by sources other than MJO convection. This result also indicates that the initiation process of the tropical intraseasonal M_r anomaly is important to understand the variability in the development of the globally integrated AAM anomaly associated with the MJO.

3.2. AAM Budget Analysis

This section examines the results of AAM budget analysis and discusses the processes that contribute to the development of the intraseasonal AAM anomaly in the tropics. Figure 4 shows

the intraseasonal M_r time tendency estimated by calculating its finite difference in time, the estimated M_r tendency as sum of all the terms on rhs of (2), and the residual as defined as the difference between the two M_r tendencies. During both the easterly and westerly wind events, the sum of budget terms captures the general temporal phase and amplitude of equatorial intraseasonal AAM anomalies.

Figure 5 shows the intraseasonal anomaly of the terms on the rhs of (2) composited with time lags on the easterly and westerly wind events and the difference between the two. Coriolis torque is not shown here since its contribution near the equator is negligible. The transport term precedes and dominates the development of equatorial intraseasonal M_r anomaly during both the easterly and westerly wind events (Fig. 5a, b). The transport term also dominates contributions to the difference between the two sets of events (Fig. 5c). The mountain torque tends to follow in quadrature to the transport term, yielding a slight delay in the net M_r tendency. Friction torque tends to be out of phase with the mountain torque, but its contribution is one order of magnitude smaller than the other two terms. This result shows that the transport term dominates the intraseasonal M_r development in the tropics and the mountain torques play a secondary role. In other words, the equatorial intraseasonal M_r does not develop through the exchange of the AAM with the solid earth, but rather develops from the intraseasonal atmospheric distribution of m_r.

The transport term is further decomposed into advection by zonal-mean winds and flux convergence by eddies as shown in (5). Figure 6 shows the three major terms driven by interactions between background and intraseasonal winds that dominate the intraseasonal anomaly of the total transport term: the zonal-mean meridional and vertical advection

$(-\{[\overline{v}]\partial[m_r^*]/\partial y + [v^*]\partial[\overline{m}_r]/\partial y\}, -\{[\dot{E}]\partial[m_r^*]/\partial p + [\dot{E}^*]\partial[\overline{m}_r]/\partial p\})$ and meridional flux convergence $(-\{\partial([<\overline{v}><m_r^*>]+[<v^*><\overline{m}_r>])/\partial y\})$. Consistent with previous studies (Weickmann *et al.,* 1997; Sakaeda and Roundy, 2014), equatorial intraseasonal M_r development is dominated by the meridional flux convergence that results from interaction between the background and intraseasonal winds. Figures 6c and 5c show that the difference in the equatorial AAM anomaly between the easterly and westerly wind events mainly results from the difference in the meridional flux convergence, suggesting that momentum transport between the tropics and subtropics by eddies is important in the development of intraseasonal M_r anomaly in the tropics.

To further examine the source region of the meridional flux convergence, the longitudinal distribution of vertically integrated meridional flux convergence and its zonally integrated quantity are shown in Fig. 7. During both the easterly and westerly wind events, there are two major sources of easterly acceleration by the meridional flux convergence that dominate its zonally integrated quantity: 1) over the Indian basin through the western Pacific (90°E-150°E) and 2) over the central Pacific basin near the dateline. The meridional flux convergence over the Indian and western Pacific basins propagates eastward at the same speed as the MJO convection. At the same time, the meridional flux convergence over the central Pacific basin contributes to the M_r in a manner that seems to be independent from the meridional flux convergence over the Indian and western Pacific basins. The main difference in the meridional flux convergence between the easterly and westerly wind events occurs over the central and east Pacific basin (Fig. 7c), while the meridional flux convergence over the Indian and western Pacific basins is not significantly different. Stronger westerly acceleration by the meridional flux convergence

persists over the eastern Pacific basin in the westerly wind events, which delays the development of negative M_r anomaly.

In order to examine which vertical levels provide an important source of the meridional flux convergence, Fig. 8 shows latitude and pressure cross sections of the zonally integrated meridional flux convergence on day −7 when the difference in the meridional flux convergence between the easterly and westerly wind events maximizes. The meridional flux convergence in the upper-tropospheric layer (300-100hPa) dominates its vertically-integrated quantity (Fig. 8a, b). The difference in the meridional flux convergence between the easterly and westerly wind events also is greatest in the upper-tropospheric layer (Fig. 8c). The combined results from Fig. 7 and Fig. 8 suggest that the upper-troposphere is the most important layer of meridional flux convergence, and it dominates driving the tropical intraseasonal M_r anomaly. The difference in this flux convergence over the central and eastern Pacific basin drives the difference in the intraseasonal equatorial M_r anomaly between the easterly and westerly wind events.

The meridional flux convergence of m_r at 125-hPa, the level of maximum difference in the meridional flux convergence, is examined in more detail to understand what drives the difference in the upper-troposphere of the central and eastern Pacific basins. Figure 9 shows the plan-view composites of 125-hPa meridional eddy flux convergence in shading and intraseasonal eddy streamfunction anomaly in black contours on the same day as Fig. 8. As shown by Weickmann *et al.* (1997) and Sakaeda and Roundy (2014), the meridional flux convergence in the tropics results from changes in the strength of the background eddy circulation by the intraseasonal circulation. Upper-tropospheric background eddies, including a pair of subtropical anticyclones

about the equator over the Eastern Hemisphere and a pair of subtropical cyclones over the east Pacific basin (see Fig. 12a of Sakaeda and Roundy, 2014) induce westerly acceleration in the tropics (Lee 1999). On day −7, the envelope of suppressed MJO convection is over the eastern Indian Ocean through the Maritime Continent (Fig. 2), suppressing the total convection in the climatologically active regions of convection. The suppressed MJO convection over the region induces a subtropical eddy circulation that is generally out of phase with the background eddy circulation (i.e., a pair of anomalous cyclones over the Eastern Hemisphere and anticyclones in the central to eastern Pacific basins), resulting in weakening of total eddy circulation and induction of anomalous easterly acceleration by the meridional flux divergence in the tropics. The pair of anomalous cyclones that are on the west of the suppressed convection over the Eastern Hemisphere induce the equatorial easterly acceleration that propagates with the convection as seen in Fig. 7. The difference in the circulation between the easterly and westerly wind events occurs mainly over the southern tropical to subtropical central and eastern Pacific basins (Fig. 9c). A pair of cyclones appears over the southeastern tropical Pacific basin during the westerly wind events, which induces anomalous westerly acceleration by strengthening the total cyclonic circulation. The northeast-to-southwest tilts of the wave train over the south tropical east Pacific basin suggest that they develop from equatorward energy dispersion of midlatitude wave trains.

In order to examine the midlatitude wave activity, wave activity flux vectors for intraseasonal winds are calculated as by Takaya and Nakamura (2001) for stationary eddies and composited on day −7 of the easterly and westerly wind events (Fig. 10). In the south central Pacific basin, the

wave flux vectors indicate equatorward propagation of wave energy and poleward refraction of the waves farther east in both the easterly and westerly wind events. A significant difference in the wave flux activity between the easterly and westerly wind events occurs from 150°W to 100°W in the southern subtropics (Fig. 10c). This difference indicates that equatorward propagation of midlatitude waves from the Southern Hemisphere is more enhanced during the westerly wind events than during the easterly wind events. This enhanced equatorward propagation leads to anomalous westerly momentum transport near the equator that is shown in Fig. 9b and delays the development of the negative M_r anomaly. These results suggest that the midlatitude waves substantially impact partly induce the variability in the equatorial intraseasonal AAM anomalies.

The AAM budget analysis shows that the upper-tropospheric meridional flux convergence induced by the modulation of background eddies by intraseasonal eddies over the Indian through the central Pacific basins is the main driver of the tropical intraseasonal M_r anomaly. This mechanism is different from one that develops the intraseasonal upper-tropospheric zonal wind over the WH. Sakaeda and Roundy (2015a) found that zonal advection is important to the initial development and amplification of intraseasonal zonal wind over the upper-troposphere of the WH, but this zonal redistribution of the momentum does not contribute to the changes in the zonally integrated momentum. If the tropical M_r is mainly driven by the development of the upper-tropospheric zonal wind over the WH, then the main driver of the AAM, the meridional flux convergence, should induce strong zonal acceleration over the WH around the same days of peak AAM acceleration. Around day −7, local easterly acceleration of the upper-tropospheric

zonal wind over the eastern Pacific basin maximizes in the easterly wind events (see Sakaeda and Roundy, 2015a), but Fig. 9a shows that the meridional flux convergence does not induce any easterly acceleration over the east Pacific basin. Instead, Sakaeda and Roundy (2015a) showed that the equatorial easterly wind associated with the pair of anticyclones over the central Pacific basin is advected eastward by the background equatorial westerly wind in a manner that accelerates intraseasonal easterly wind over the east Pacific basin. This equatorial easterly wind continues to propagate eastward and amplify over the eastern Pacific and Atlantic basins, but the amplification of this local zonal wind over these regions does not directly drive the tropical AAM anomaly. The simultaneous development of AAM and upper-tropospheric zonal wind over the WH appear because they share the same source phenomena, which is the subtropical eddies, but they develop through different specific mechanisms. The subtropical eddies transport momentum poleward from the equator, inducing the negative M_r anomaly in the tropics, while the equatorial zonal wind associated with the subtropical eddies propagates eastward and locally amplifies over the east Pacific basins through zonal advection of background zonal wind.

3.3. The Impacts of AAM on MJO Convection

This section examines the impact of the equatorial AAM on the subsequent development of MJO convection over the Indian Ocean. In order to separate the effects of local upper-tropospheric zonal wind over the WH and the AAM anomalies, the WH Zonal Wind Index from Sakaeda and Roundy (2015a) is recalculated using 200-hPa intraseasonal zonal wind anomaly after removing its zonal-mean component at each latitude. This eddy (zonally asymmetric) 200-

hPa intraseasonal zonal wind anomaly is averaged from 2.5°N to 2.5°S and 140°W to 40°W to represent the local upper-tropospheric intraseasonal zonal wind anomaly over the WH. The resulting time series is referred to as the Eddy WH Zonal Wind Index (EWHZI).

Table 1 shows the decomposition of the identified MJO convective initiation events (in phase 1) by the signs of equatorial intraseasonal M_r anomaly (averaged from 5°N to 5°S) and the EWHZI. During the convective initiation of the MJO identified by the method described in Section 2.2 (also by Sakaeda and Roundy, 2015a), 73% of the events have local easterly wind anomaly in the upper-troposphere of the WH while 27% have westerly wind anomaly. The events have less preference for states of the equatorial M_r (53% negative AAM and 47% positive AAM).

Figure 11 shows scatter plots between the AAM and EWHZI during the phase 1 events, with shading of the plotted points indicating the intraseasonal OLR anomaly over the Indian Ocean. The axes show the amplitude of the EWHZI and AAM on day 0 and the shading shows the amplitude of intraseasonal OLR anomaly averaged over 10°N-10°S and 75°E-105°E prior to and after the events. The distribution of the AAM and the EWHZI show that both of their signs are skewed toward their negative values during phase 1, but there is no significant linear relationship between the EWHZI and AAM. Prior to the events (days −5 to 0, Fig. 11a), the amplitude of the OLR anomaly tends to be nearly zero or weakly positive and does not have any apparent relationship with the AAM or EWHZI. On days 5 to 10 (Fig. 11b), most of the events indicate that development of suppressed convection and its amplitude tends to be stronger following negative EWHZI and AAM anomalies. This result is consistent with Roundy (2014) and Sakaeda

and Roundy (2015a), who showed that MJO convection tends to subsequently develop stronger and better-organized envelopes of convection following the events with the WH upper-tropospheric easterly wind, but Fig. 11 suggests that it tends to occur especially when the equatorial intraseasonal M_r anomaly is also negative. Figure 11 suggests that within the events with the negative EWHZI, the ones with negative M_r anomaly tend to develop stronger MJO convection. However, during the events with positive M_r anomaly, the sign of the EWHZI does not seem to have much impact on the subsequent development of MJO convection. These results suggest that the association of the WH upper-tropospheric zonal wind with the subsequent development of MJO convection by Sakaeda and Roundy (2015a) is enhanced when the intraseasonal M_r anomaly is also negative.

In order to assess the potential impacts of the M_r anomaly on MJO convection, the events with negative EWHZI are stratified by the sign of the AAM anomaly. The negative EWHZI events with positive and negative intraseasonal M_r anomalies are referred to hereafter as positive AAM events (events that fall within the top left quadrant of Fig. 11) and negative AAM events (bottom left quadrant of Fig. 11), and their differences are examined. The mean value of the EWHZI is not statistically significantly different between the positive and negative AAM events. Therefore, the difference in circulation between the positive and negative AAM events must be associated with the equatorial M_r (although the total intraseasonal zonal wind over the upper-troposphere of the WH would have stronger amplitude in the negative AAM events due to the presence of a negative M_r anomaly that is excluded from the EWHZI).

Figure 12 shows the evolution of intraseasonal OLR anomaly and AAM during the negative and positive AAM events, and the difference between the two sets of events. In both sets of events, the convectively enhanced envelope of the MJO initiates over the Indian Ocean around day 0 and propagates eastward, but the amplitude of the convection is significantly stronger in the negative AAM events over the Indian Ocean from days 3 through 12 (labelled A in Fig. 12c). Some significant differences in MJO convection between the two means also occur over the central Pacific basin (labelled B in Fig. 12c). MJO convection during the positive AAM events tends to be more active there than during the negative AAM events over the central Pacific basin. Enhanced MJO convective activity over the central Pacific basin is often observed during the warm phase of El Niño Southern Oscillation (ENSO) when anomalously high sea surface temperature (SST) is observed in the central and eastern Pacific basins (Kessler, 2001; Vincent *et al.,* 1998). Consistent with the previous findings on the relationship between MJO convection and ENSO, low-frequency anomaly (periods longer than 100 days) of SST tends to be anomalously high over the central and eastern Pacific basins during the positive AAM events (Fig. 13) when MJO convection is more active over the central Pacific basin. However, the monthly Niño 3.4 index obtained from Climate Prediction Center is less than or equal to zero consistent with neutral to cold ENSO states about 30% of the time during the months of positive AAM events (not shown), suggesting that the warm phase of ENSO is a favorable but not required background state for the positive AAM events to occur. No significant low-frequency SST anomaly appears about the equator during the negative AAM events. To further investigate the potential relationship between ENSO and MJO convective activity over the Indian Ocean,

interannual variability of the intraseasonal OLR is calculated following Kessler (2001), by applying one year running means to smooth the squared intraseasonal OLR anomaly and then taking the square root of the result. The interannual variability of intraseasonal OLR activity over the Indian Ocean (10°N-10°S, 75°E-105°E) and the low-frequency SST anomaly over the east Pacific basin are significantly negatively correlated (not shown), suggesting that MJO convective activity over the Indian Ocean tends to be suppressed during the warm phase of ENSO. However, the interannual variability of intraseasonal OLR anomaly over the Indian Ocean is not significantly correlated with the local low-frequency SST anomaly in the Indian Ocean. Okumura and Deser (2010) also show that the association between the Indian basin SST and ENSO varies subseasonally. These results suggest that the warm phase of ENSO is associated with the weaker MJO convective activity over the Indian Ocean, but the impact of ENSO on MJO convective activity over the Indian basin is not through the impact of the Indian basin SST by ENSO.

During the positive AAM events, low-frequency SST anomaly averages slightly positive in the Indian Ocean (Fig. 13b). However, the MJO tends to develop weaker envelopes of convection over the Indian Ocean during the positive AAM events (Fig. 12), suggesting that other processes must overwhelm the positive effect of higher background SST by suppressing MJO convection during the positive AAM events. The higher SST may also be a result of the suppression of convection that increases the amount of solar radiation reaching the surface. However, no significant mean low-frequency OLR anomalies occur in the same population of events over the Indian Ocean. Therefore the suppression of MJO convective activity over the

Indian basin during the warm phase of ENSO may results through its impact on atmospheric circulation, which prefers positive AAM anomalies during the convective initiation of the MJO over the Indian basin.

Sakaeda and Roundy (2015b) suggested that the upper-tropospheric intraseasonal zonal wind can impact the subsequent development of MJO convection by suppressing or enhancing the upper-tropospheric divergence and therefore the ventilation of the overturning circulation associated with initiating MJO convection over the Indian basin. This mechanism may also help explain the difference in the strength of MJO convection during the negative and positive AAM events. The left column of Fig. 14 shows the zonal cross sections of intraseasonal zonal wind and its divergence on day 0 of the negative AAM events, positive AAM events, and their difference over the Indian basin. The persistence of westerly wind anomalies in the mid- to upper-troposphere is associated with significantly stronger mid-tropospheric convergence in the positive AAM events between 60°E and 90°E. The zonal wind anomalies in the upper-troposphere tilt eastward with height and Sakaeda and Roundy (2015b) showed that these zonal wind anomalies tend to be in phase with geopotential height anomalies, resembling the theoretical and observed structure of a Kelvin wave associated with MJO convection (Wallace and Kousky, 1968; Kiladis *et al*., 2001; Zhou and Holton, 2002). Therefore the difference in the mid-tropospheric zonal divergence between the negative and positive AAM events is associated with the difference in the strength and arrival timing of the Kelvin wave. On day 7 (right column of Fig. 14), this mid-tropospheric convergence persists in the positive AAM events, while the

lower-tropospheric convergence and upper-tropospheric divergence are aligned vertically in the negative AAM events, associated with an enhanced overturning deep convective circulation.

These results suggest that the suppression of lower-tropospheric ascent due to the persistence of mid-tropospheric horizontal convergence leads to weaker MJO convection in the positive AAM events. This mid-tropospheric convergence apparently persists due to the strengthened mid- to upper-tropospheric westerly wind anomaly associated with Kelvin wave in the presence of intraseasonal positive M_r on the equator. Therefore, the arrival timing and strength of mid- to upper-tropospheric intraseasonal zonal wind and its associated horizontal divergence can influence the strength of initiating MJO convection over the Indian Ocean by suppressing or enhancing large-scale ascent within the envelope of initiating convection. The state of the intraseasonal AAM anomalies can influence the subsequent development of initiating MJO convection over the Indian basin by influencing the arrival timing and strength of upper-tropospheric intraseasonal zonal wind over the basin. The difference in the evolution of M_r between the negative and positive AAM events is also largely driven by the meridional flux convergence in the WH upper-troposphere (not shown), suggesting that the WH is the greatest source of variability in the state of the equatorial M_r anomaly during the convective initiation of the MJO over the Indian Ocean.

4. Conclusion

The first part of this study examines the dynamical relationship between the upper-tropospheric intraseasonal zonal wind in the WH and relative atmospheric angular momentum

M_r anomaly that tend to evolve simultaneously. MJO convective initiation events are stratified by the signs of the upper-tropospheric intraseasonal zonal wind over the WH. Then, the driving mechanisms of the equatorial M_r anomaly during those events are examined by using budget analysis. The main driver of the equatorial M_r anomaly is the upper-tropospheric meridional flux convergence that results from the modulation of background subtropical eddies by the intraseasonal eddy circulation, while mountain torque plays a secondary role. There are generally two major source regions of zonal momentum transport by the meridional flux convergence: 1) the Indian to west Pacific basins and 2) the central to eastern Pacific basins. The central and eastern Pacific region is the greater source of variability in the state of equatorial intraseasonal M_r anomaly during the convective initiation of the MJO. The difference in the intraseasonal M_r anomaly between the easterly and westerly wind events results from enhanced equatorward propagation of midlatitude intraseasonal wave trains from the Southern Hemisphere over the tropical east Pacific basin during the westerly wind events, which transports anomalous positive zonal momentum onto the equator and delays the development of the negative intraseasonal M_r anomaly.

The main driving mechanism of the equatorial intraseasonal M_r anomaly is different from the driving mechanism of the upper-tropospheric intraseasonal zonal wind over the WH found by Sakaeda and Roundy (2015a), where zonal advection plays a more significant role. However, while the driving mechanisms are different, both the equatorial intraseasonal M_r and upper-tropospheric zonal wind anomalies are associated with the subtropical eddies. The subtropical eddies transport intraseasonal zonal momentum into or out of the tropics through the meridional

flux convergence or divergence, thereby driving the changes in the equatorial intraseasonal M_r anomaly. At the same time, the equatorial zonal wind associated with the same subtropical eddies over the central Pacific basin is advected eastward and amplified over the east Pacific basin through the advection of background zonal wind (Sakaeda and Roundy, 2015a). Therefore, the equatorial intraseasonal M_r and the WH upper-tropospheric zonal wind anomalies develop simultaneously due to their common source phenomena that transport momentum, but they are driven by different mechanisms from those sources.

The second part of this study examines the influence of intraseasonal M_r anomalies on the subsequent development of MJO convection over the Indian Ocean. Within the MJO convective initiation events with intraseasonal upper-tropospheric easterly wind anomaly in the WH, the ones with negative equatorial M_r anomalies (referred to as negative AAM events) subsequently develop significantly stronger envelopes of enhanced MJO convection over the Indian Ocean than the events with positive M_r anomaly (positive AAM events). The difference in the strength of the convection between these sets of events seems to result from the difference in the mid- to upper-tropospheric circumnavigating zonal wind associated with Kelvin waves. During the positive AAM events, westerly wind anomalies persist over the western Indian basin in the mid- to upper-troposphere, inducing mid-tropospheric convergence and suppressing the lower-tropospheric ascent.

Our results suggest that the part of the variability in the strength and characteristics of MJO convection over the Indian Ocean could be generated by the combined variability in the circumnavigating circulation from the WH and the state of equatorial AAM. Sakaeda and

Roundy (2015a, b) showed that this circumnavigating circulation does not propagate with a consistent structure or dynamics across all longitudes. Sakaeda and Roundy (2015a) showed that before the upper-tropospheric Kelvin wave generated by MJO convection over the warm pool reaches the east Pacific basin, upper-tropospheric intraseasonal zonal wind anomalies develop there in association with midlatitude circulations intruding on the tropics, which can influence the strength and arrival timing of the circumnavigating circulation to the Indian Ocean. Intrusion of midlatitude waves is also suggested to play a part in the formation of the Kelvin wave structure as the circumnavigating circulation propagates from east Pacific to the Atlantic basin (Sakaeda and Roundy, 2015b) The meridional exchange of zonal momentum with the subtropics can also influence the strength of the circumnavigating zonal wind by modulating the equatorial AAM anomaly. Therefore the interaction with the subtropical and midlatitude circulations can influence the evolution of the circumnavigating zonal wind over the WH by modulating the AAM or the local WH upper-tropospheric zonal wind, which then influence the subsequent development of initiation convection of the MJO over the Indian Ocean.

The remote association between the interannual variability of MJO convection over the Indian Ocean and ENSO may also result from the modulation of the WH intraseasonal circulation by ENSO. MJO convection tends to be more active over the central Pacific basin during the warm phase of ENSO (Kessler, 2001), and Sakaeda and Roundy (2015a) showed that the longer persistence of enhanced MJO convection over the central Pacific basin tends to be associated with westerly wind anomalies over the east Pacific basin during the convective initiation of the MJO over the Indian Ocean. Therefore, the warm phase of ENSO would tend to

remotely suppress MJO convection over the Indian Ocean by favoring the persistence of the westerly wind anomaly over the WH at the time of convective initiation over the Indian Ocean, which then suppresses the strength of convection. Some questions remain to be answered in future studies. These include understanding the causes of variability in the intraseasonal midlatitude wave propagation into the equator over the east Pacific basin, which tends to result in the variability in the development of equatorial AAM associated with the MJO. While this study suggests that the WH upper-tropospheric zonal wind anomalies influence the development of MJO convection by enhancing or suppressing the upper-tropospheric divergence and ventilation of initiating MJO convection, it is of interest to explore how the circumnavigating zonal wind from the WH may influence the other suggested sources of intraseasonal instability such as cloud-radiation feedbacks (e.g., Bony and Emanuel, 2005), wind-evaporation feedbacks (e.g., Emanuel, 1987) and upscale momentum and heat transports from synoptic or mesoscale scales embedded within MJO convection (e.g., Biello and Majda, 2005; Majda and Stechman, 2009). Further investigation is needed to deepen our understanding of the role of circumnavigating tropical and extratropical circulations from the WH on to the development of MJO convection over the Indian Ocean.

Acknowledgements

We thank two anomalous reviewers for their helpful comments. This work was supported by NSF grant numbers AGS1358214 and AGS1128779.

References

Anderson JR, Rosen RD. 1983. The latitude-height structure of 40–50 day variations in atmospheric angular momentum. *J. Atmos. Sci.* **40** : 1584–1591.

Biello JA, Majda AJ. 2005. A new multiscale model for the Madden–Julian oscillation. *J. Atmos. Sci.* **62** : 1694–1721.

Bony S, Emanuel KA. 2005. On the role of moist processes in tropical intraseasonal variability. Cloud–radiation and moisture–convection feedbacks. *J. Atmos. Sci*. **62** : 2770–2789.

Dickey JO, Ghil M, Marcus SL. 1991. Extratropical aspects of the 40-50 day oscillation in length-of-day and atmospheric angular momentum. *J. Geophys. Res*. **96** : 22643-22658.

Emanuel KA. 1987. An air–sea interaction model of intraseasonal oscillations in the tropics. *J. Atmos. Sci.* **44** : 2324–2340.

Feldstein SB, Lee S. 1995. The intraseasonal evolution of angular momentum in aquaplanct and realistic GCMs. *J. Atmos. Sci.* **52** : 625–649.

Gill AE. 1980. Some simple solutions for heat-induced tropical circuclation. *Quart. J. R. Met. Soc.* **106** : 447-462.

Guzler DS, Ponte RM. 1990. Exchange of momentum among atmosphere, ocean, and solid earth associated with the Madden-Julian oscillation. *J. Geophys. Res*. **95** : 18679-18686.

Hoskins BJ, Ambrizzi T. 1993. Rossby wave propagation on a realistic longitudinally varying flow. *J. Atmos. Sci.* **50** : 1661-1671.

Kang IS, Lau KM. 1994. Principal modes of atmospheric circulation anomalies associated with global angular momentum fluctuations. *J. Atmos. Sci.* **51** : 1194–1205.

Kessler WS. 2001. EOF Representations of the Madden–Julian Oscillation and Its Connection with ENSO. *J. Climate*. **14** : 3055–3061.

Kiladis GN, Straub KH, Haertel PT. 2005. Zonal and vertical structure of the Madden-Julian oscillation. *J. Atmos. Sci*. **62** : 2790-2809.

Kiladis GN, Straub KH, Reid GC, Gage KS. 2001. Aspects of interannual and intraseasonal variability of the tropopause and lower stratosphere. *Quart. J. Roy. Meteor. Soc.* **127** : 1961-1983.

Lee S, Son SW, Grise K, Feldstein SB. 2007. A mechanism for the poleward propagation of zonal mean flow anomalies. *J. Atmos. Sci*. **64** : 849–868.

Lee S. 1999. Why are the climatological zonal winds easterly in the equatorial upper troposphere? *J. Atmos. Sci.* **56** : 1353–1363.

Liebmann B, Smith CA. 1996. Description of a complete (interpolated) outgoing longwave radiation dataset. *Bull. Amer. Meteor. Soc*. **77** : 1275-1277.

MacRitchie K, Roundy PE. 2015. The two-way relationship between the Madden Julian oscillation and anticyclonic wave breaking. *Quart. J. R. Met. Soc.* submitted.

Madden RA, Speth P. 1995. Estimates of atmospheric angular momentum, friction, and mountain torques during 1987–1988. *J. Atmos. Sci.* **52** : 3681–3694.

Madden RA. 1987. Relationships between changes in the length of day and the 40 to 50 day oscillation in the tropics. *J. Geophys. Res*. **92** : 8391-8399.

Madden RA. 1988. Large intraseasonal variations in wind stress over the tropical Pacific. *J. Geophys. Res*. **93** : 5333-5340.

Magana V. 1993. The 40- and 50-day oscillations in atmospheric angular momentum at latitudes. *J. Geophys. Res*. **98** : 10441-10450.

Majda AJ, Stechmann SN. 2009. The skeleton of tropical intraseasonal oscillations. *Proc. Natl. Acad. Sci. U. S. A.* **106** : 8417-8422.

Marcus SL, Ghil M, Dickey JO. 1994. The extratropical 40-day oscillation in the UCLA general circulation model. Part I. atmospheric angular momentum. *J. Atmos. Sci.* **51** : 1431–1446.

Matthews AJ. 2000. Propagation mechanisms for the Madden-Julian Oscillation. *Quart. J. Roy. Meteor. Soc.* **126** : 2637-2652.

Matthews AJ. 2008. Primary and successive events in the Madden-Julian Oscillation. *Quart. J. Roy. Meteor. Soc.* **134** : 439-453.

Milliff RF, Madden RA. 1996. The Existence and Vertical Structure of Fast, Eastward-Moving Disturbances in the Equatorial Troposphere. *J. Atmos. Sci.* **53** : 586–597.

Moore RW, Martius O, Spengler T. 2010. The modulation of the subtropical and extratropical atmosphere in the Pacific basin in response to the Madden-Julian oscillation. *Mon. Wea. Rev*. **138** : 2761-2779.

Okumura YM, Deser C. 2010. Asymmetry in the Duration of El Niño and La Niña. *J. Climate*. **23** : 5826–5843.

Roundy PE. 2014. Some aspects of Western Hemisphere circulation and the Madden–Julian Oscillation. *J. Atmos. Sci.* **71** : 2027–2039.

Saha S, Coauthors. 2010. The NCEP climate forecast system reanalysis. *Bull. Amer. Mteor. Soc.* **91** : 1015-1057.

Sakaeda N, Roundy PE. 2014. The role of interactions between multiscale circulations on the observed zonally averaged zonal wind variability associated with the Madden–Julian Oscillation. *J. Atmos. Sci.* **71** : 3816–3836.

Sakaeda N, Roundy PE. 2015a. The development of upper-tropospheric wind over the Western Hemisphere in association with MJO convective initiation. *J. Atmos. Sci*. **72** : 3138–3160.Sakaeda N, Roundy PE. 2015b. The Development of Upper-Tropospheric Geopotential Height Anomaly in the Western Hemisphere during MJO Convective Initiations. *Q.J.R. Meteorol. Soc.* in press. doi:10.1002/qj.2696.

Salby ML, Garcia RR, Hendon HH. 1994. Planetary-scale circulations in the presence of climatological and wave-induced heating. *J. Atmos. Sci.* **51** : 2344-2367.

Salby ML, Hendon HH. 1994. Intraseasonal behavior of clouds, temperature, and motion in the Tropics. *J. Atmos. Sci.*. **51** : 2207–2224.

Sobel A, Kim D. 2012. The MJO-Kelvin wave transition. *Geophys. Res. Lett.* **39**, L20808, doi.10.1029/2012GL053380.

Takaya K, Nakamura H. 2001. A formulation of a phase-independent wave-activity flux for stationary and migratory quasigeostrophic eddies on a zonally varying basic flow. *J. Atmos. Sci.* **58** : 608–627.

Vincent DG, Fink A, Schrage JM, Speth P. 1998. High- and Low-Frequency Intraseasonal Variance of OLR on Annual and ENSO Timescales. *J. Climate*, **11**, 968–986.

Wallace JM, Kousky VE. 1968. Observational evidence of kelvin waves in the tropical stratosphere. *J. Atmos. Sci.* **25** : 900–907.

Webster PJ, Chang HR. 1988. Equatorial Energy Accumulation and Emanation Regions: Impacts of a Zonally Varying Basic State. *J. Atmos. Sci.* **45** : 803–829.

Webster PJ, Holton JR. 1982. Cross-equatorial response to middle-latitude forcing in a zonally varying basic state. *J. Atmos. Sci.* **39** : 722–733.

Weickmann K, Berry E. 2009. The tropical Madden–Julian Oscillation and the Global Wind Oscillation. *Mon. Wea. Rev.* **137** : 1601–1614.

Weickmann KM, Khalsa SJS, Eischeid J. 1992. The atmospheric angular-momentum cycle during the tropical Madden–Julian Oscillation. *Mon. Wea. Rev.* **120** : 2252–2263.

Weickmann KM, Kiladis GN, Sardeshmukh PD. 1997. The dynamics of intraseasonal atmospheric angular momentum oscillations. *J. Atmos. Sci*. **54** : 1445–1461

Weickmann KM, Sardeshmukh PD. 1994. The atmospheric angular momentum cycle associated with a Madden–Julian Oscillation. *J. Atmos. Sci.* **51** : 3194–3208.

Weickmann KM. 2003. Mountains, the global frictional torque, and the circulation over the Pacific–North American region. *Mon. Wea. Rev.* **131** : 2608–2622.

Wheeler MC, Hendon HH. 2004. An all-season real-time multivariate MJO index. development of an index for monitoring and prediction. *Mon. Wea. Rev*. **132** : 1917-1932.

Wheeler M, Kiladis GN. 1999. Convectively coupled equatorial waves: analysis of clouds and temperature in the wavenumber-frequency domain. *J. Atmos. Sci.* **56**: 374-399.

Zhang C. 2005. Madden-Julian Oscillation. *Rev. Geophys.* **43**, RG2003, doi.10.1029/2004RG000158

Zhou X, Holton JR. 2002. Intraseasonal variations of tropical cold-point tropopause temperatures. *J. Climate*. **15** : 1460–1473.

Table List

Table 1. Number of phase 1 events categorized based on the signs of intraseasonal M_r anomaly averaged over 5°N to 5°S and Eddy Western Hemisphere Zonal Wind Index (EWHZI, calculated by averaging 200-hPa eddy intraseasonal zonal wind from 2.5°N to 2.5°S and 140°W to 40°W) on day 0. The most right column indicates total number of events based solely on the sign of EWHZI. The bottom row indicates total number of events based solely on the sign of AAM. The ratio of the number of events in each category over the total number of events is indicated in percentage inside parentheses.

Figure Captions

FIG 1. Longitude-time diagrams of 200-hPa intraseasonal zonal wind anomalies (m s^{-1}, shading) and time series of intraseasonal zonally and vertically integrated relative AAM anomalies (1.0×10^{24} kg m^2 s^{-1}) averaged from 5°N to 10°S for (a) easterly wind events, (b) westerly wind events, and (c) difference between the easterly and westerly wind events. Zonal wind anomalies with statistical significance at 95% confidence level are contoured with thin black solid line for positive values and black dashed line for negative values. The same statistical significance for the AAM anomalies is indicated by black dots.

FIG 2. Longitude-time diagrams of intraseasonal surface pressure anomaly (Pa, shading) and intraseasonal OLR anomaly contoured at every 5 W m^{-2} (solid indicates negative value and positive indicates positive value) for (a) easterly wind events, (b) westerly wind events, and (c) difference. The statistical significance of the shaded anomalies is indicated in the same manner as Fig. 1.

FIG 3. (Top) Time-series of globally integrated intraseasonal relative AAM anomaly and (bottom) time-latitude diagrams of its zonally and vertically integrated quantity (unit: 1×10^{25} kg m^2 s^{-1}). The same statistical significance as Fig.1 is indicated by black contour line.

FIG 4. Time series of (black solid) zonally and vertically integrated intraseasonal AAM time tendency ($\partial M_r / \partial t$), (black dashed) its estimated tendency as sum of the terms on rhs of (2), and (gray dashed) residual averaged over 5°N-10°S for (a) easterly wind events and (b) westerly

wind events. All AAM time tendencies are shown in the unit of Hadley. Anomalies that are statistically significantly different from zero are indicated by dots.

FIG 5. Time series of (black solid) intraseasonal AAM time tendency, AAM tendency driven by (black dashed) transport, (gray solid) mountain torque, and (grey dashed) friction torque averaged over 10°N-5°S for (a) easterly wind events, (b) westerly wind events, and (c) difference between the easterly and westerly wind events. Statistical significance of the anomalies is shown in the same manner as Fig. 4.

FIG 6. Same as Fig. 5 except showing (black solid) total transport $-\left[\{\nabla\cdot(\mathbf{v}m_r)\}\right]^*$, (black dashed) meridional advection by zonal-mean intraseasonal and background winds $-\{[\overline{v}]\partial[m_r^*]/\partial y+[v^*]\partial[\overline{m}_r]/\partial y\}$, (grey solid) vertical advection by zonal-mean intraseasonal and background winds $-\{[\acute{E}]\partial[m_r^*]/\partial p+[\acute{E}^*]\partial[\overline{m}_r]/\partial p\}$, and (grey dashed) meridional flux convergence by intraseasonal and background winds $-\{\partial([<\overline{v}><m_r^*>]+[<v^*><\overline{m}_r>])/\partial y\}$.

FIG 7. Same as Fig.1 except showing vertically integrated meridional flux convergence due to background-intraseasonal interactions $-\{\partial([<\overline{v}><m_r^*>]+[<v^*><\overline{m}_r>])/\partial y\}$ and its zonally integrated quantity are plotted in shading and profile (unit: Hadley). The statistical significances are shown in the same manners as Fig. 1.

FIG 8. Latitude-pressure composites of meridional flux convergence by background-intraseasonal interaction, $-\partial([<\overline{v}><m_r^*>]+[<v^*><\overline{m}_r>])dp/g\partial y$, (unit: Hadley) on day −7

of a) easterly wind events, b) westerly wind events, and c) difference between the two sets of events.

FIG 9. Plan view composites of 125hPa meridional flux convergence by background-intraseasonal interactions (unit: Hadley, shading), $-\partial([<\bar{v}><m_r^*>]+[<v^*><\overline{m}_r>])dp/g\partial y$, and 125hPa eddy stream function contoured every 2×10^6 m^2 s^{-1} interval (black contour, solid indicates positive and dashed indicates negative values) on day −7 of a) easterly wind events, (b) westerly wind events, and (c) difference between the two sets of events. The shaded anomalies that are statistically significantly different from zero are contoured with thin black solid line for positive values and thin black dot-dashed line for negative values.

FIG 10. Plan-view composites of 125hP intraseasonal wave flux vectors and eddy geopotential height anomaly (unit: m, shading). The wave flux vectors are only plotted poleward of 5°N or 5°S. The statistical significance of the shaded anomalies are shown in the same manner as Fig. 1.

FIG 11. Scatter plots of EWHZI against AAM on day 0 of all phase 1 events. Shading indicates the amplitude of intraseasonal OLR anomalies (W m^{-2}) averaged over 10°N-10°S and 75°E-115°E on (a) days −5 through 0 and (b) days 5 through 10. Negative OLR values are plotted with squares and positive OLR values are plotted in circles.

FIG 12. Longitude-time diagrams of intraseasonal OLR anomalies (shading) and time series of intraseasonal M_r anomalies averaged over 10°S-5°N for (a) negative AAM events, (b) positive AAM events, and (c) difference between (a) and (b). Statistical significance of the plotted anomalies is shown in the same manner as Fig. 1.

FIG 13. Low-frequency (periods longer than 100 days) SST anomaly (unit: K) of (a) negative AAM events and (b) positive AAM events. The anomalies that are statistically significantly different from zero are contoured in black solid lines for positive values and in black dashed lines for negative values.

FIG 14. Longitude-pressure diagrams of intraseasonal zonal wind anomaly (m s^{-1}, shading) and its divergence (plotted at 5×10^{-7} s^{-1} interval, black solid lines indicate positive and dashed lines indicate negative values) averaged from 10°N to 10°S (left column) at day 0 and (right column) day 7. Top row shows negative AAM events, the middle row shows the positive AAM events, and the bottom row shows the difference between the top and middle rows.

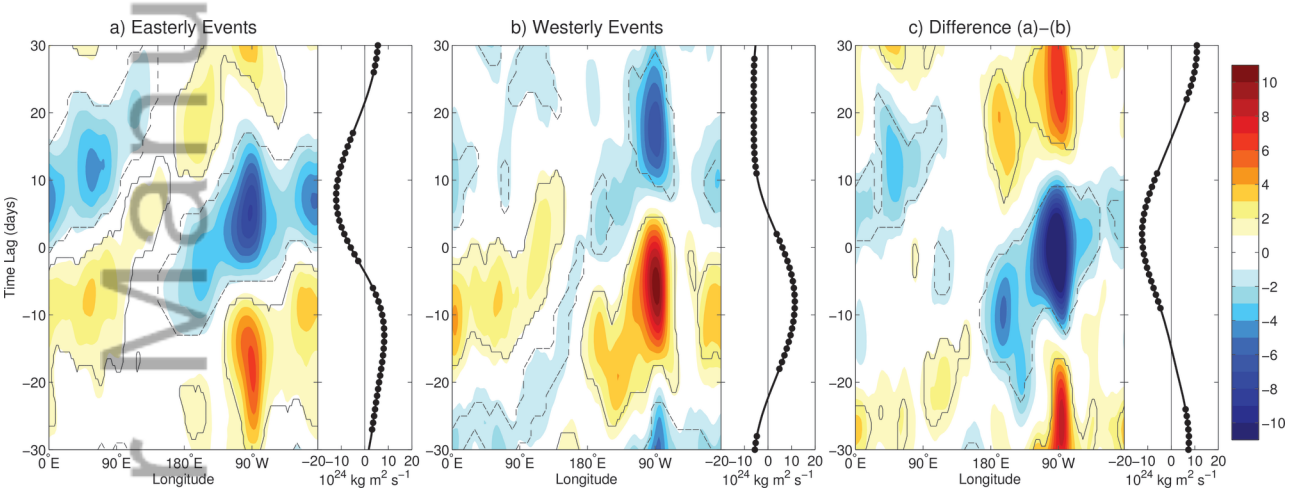

fig1_hovlon_umjo200aam

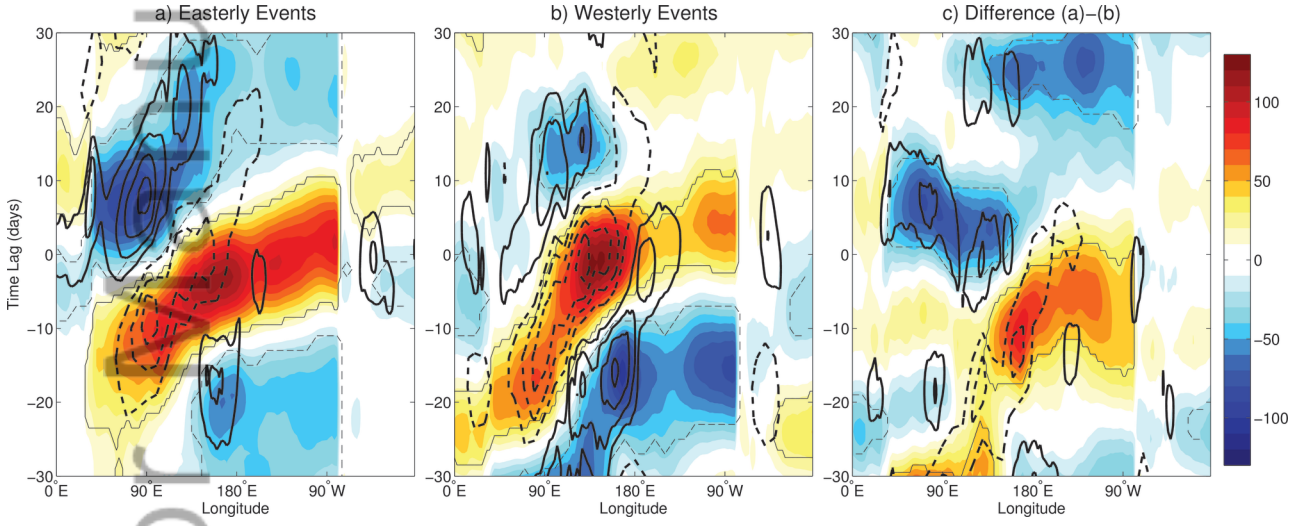

fig2_hovlon_sfpolr

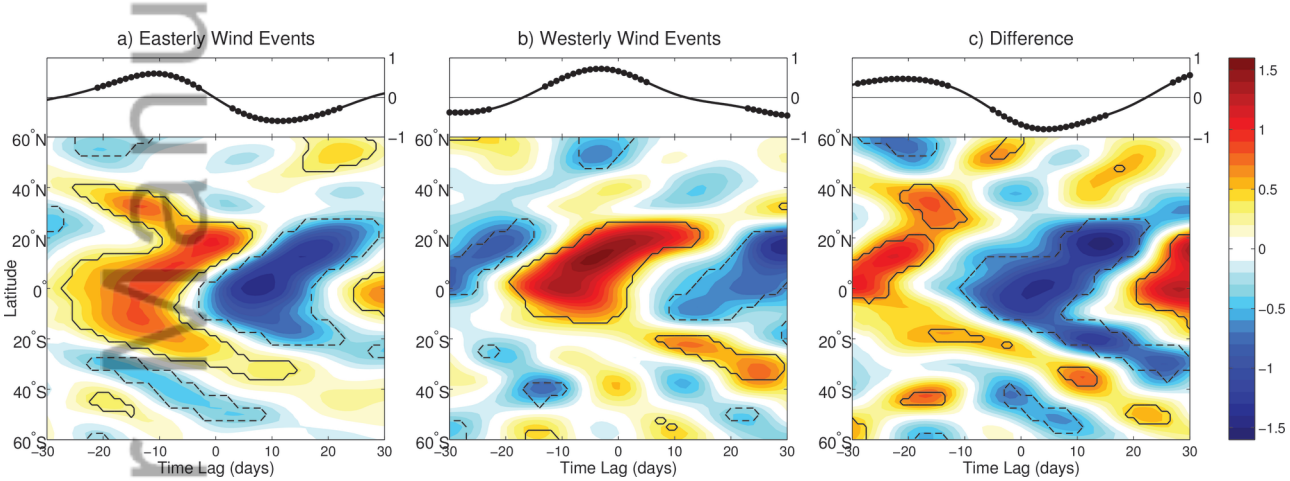

fig3_hovlat_aam

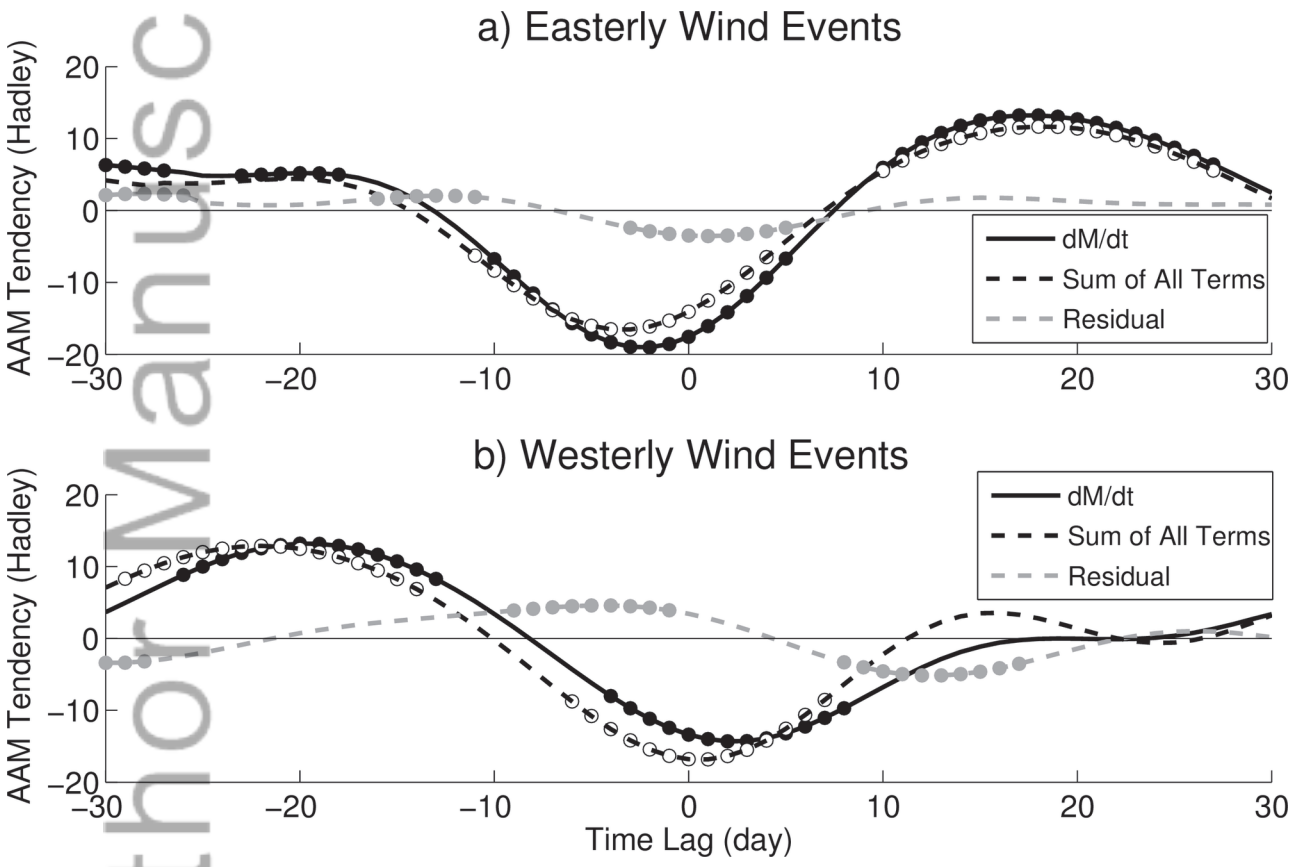

fig4_timeplot_dmdt_sum_error

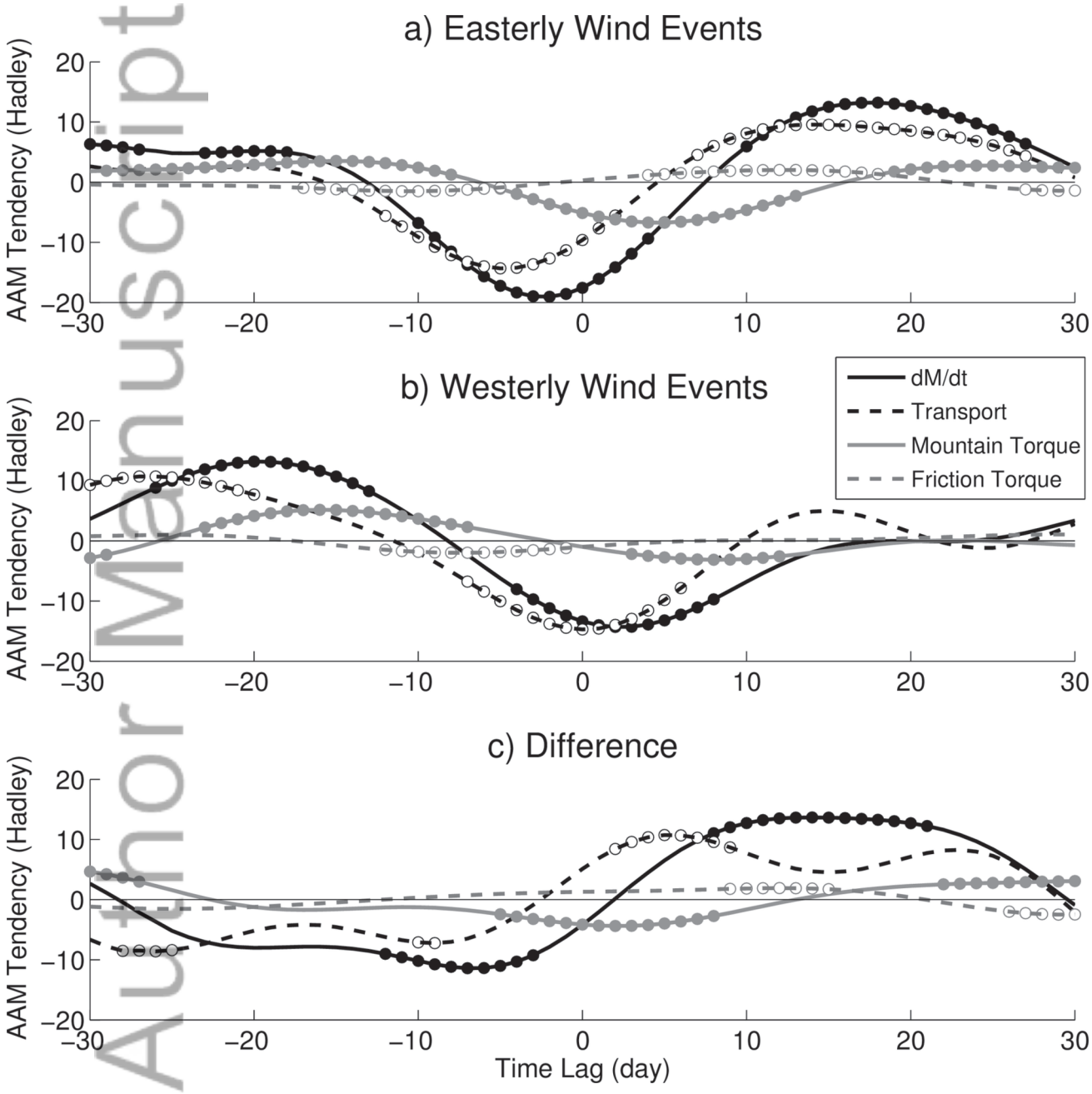

fig5_timeplot_mainterms

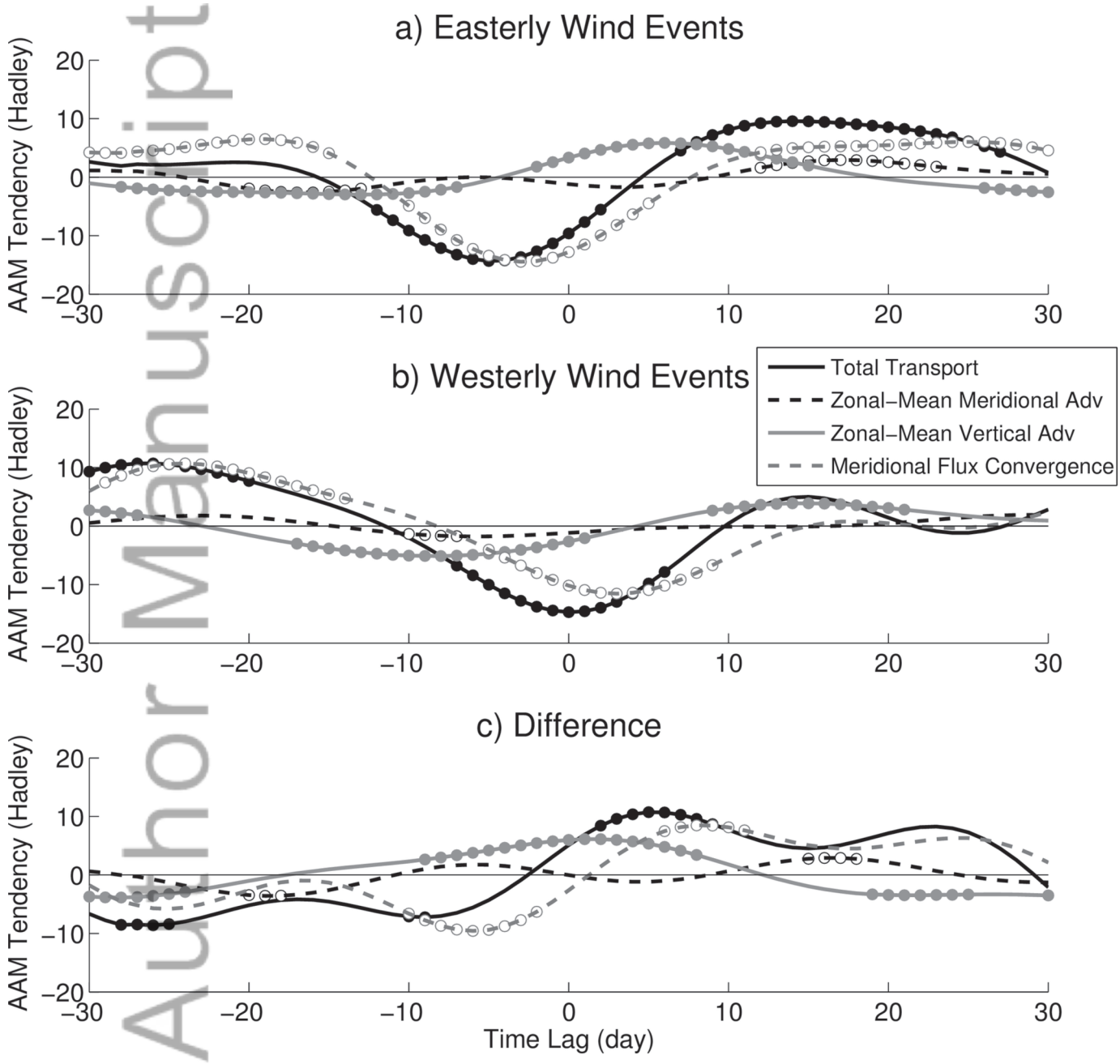

fig6_timeplot_advterms

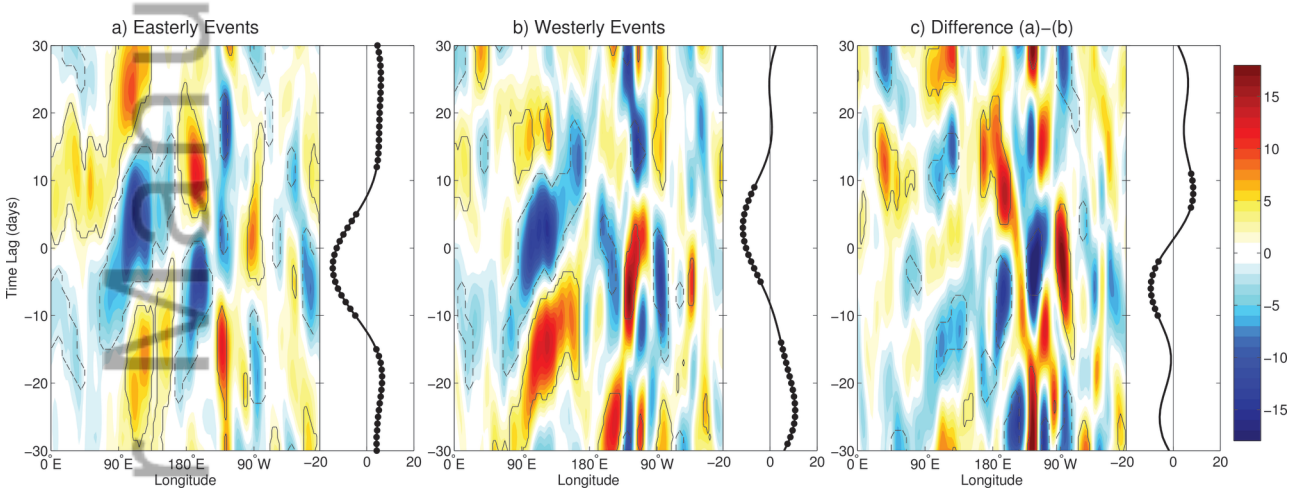

fig7_hovlon_term3b

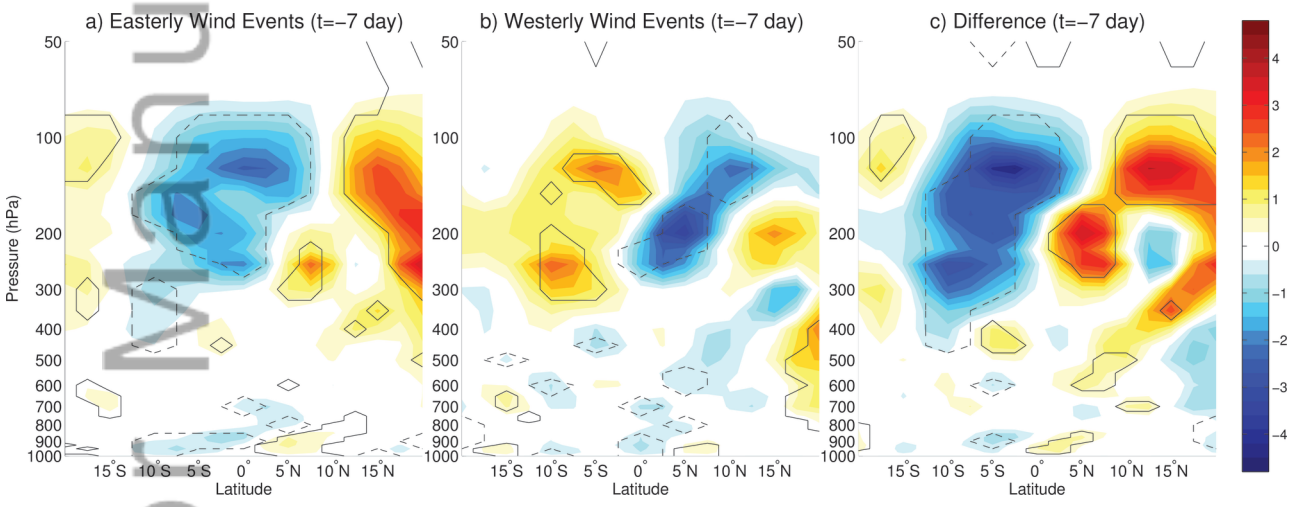

fig8_xsection_term3b_t-7

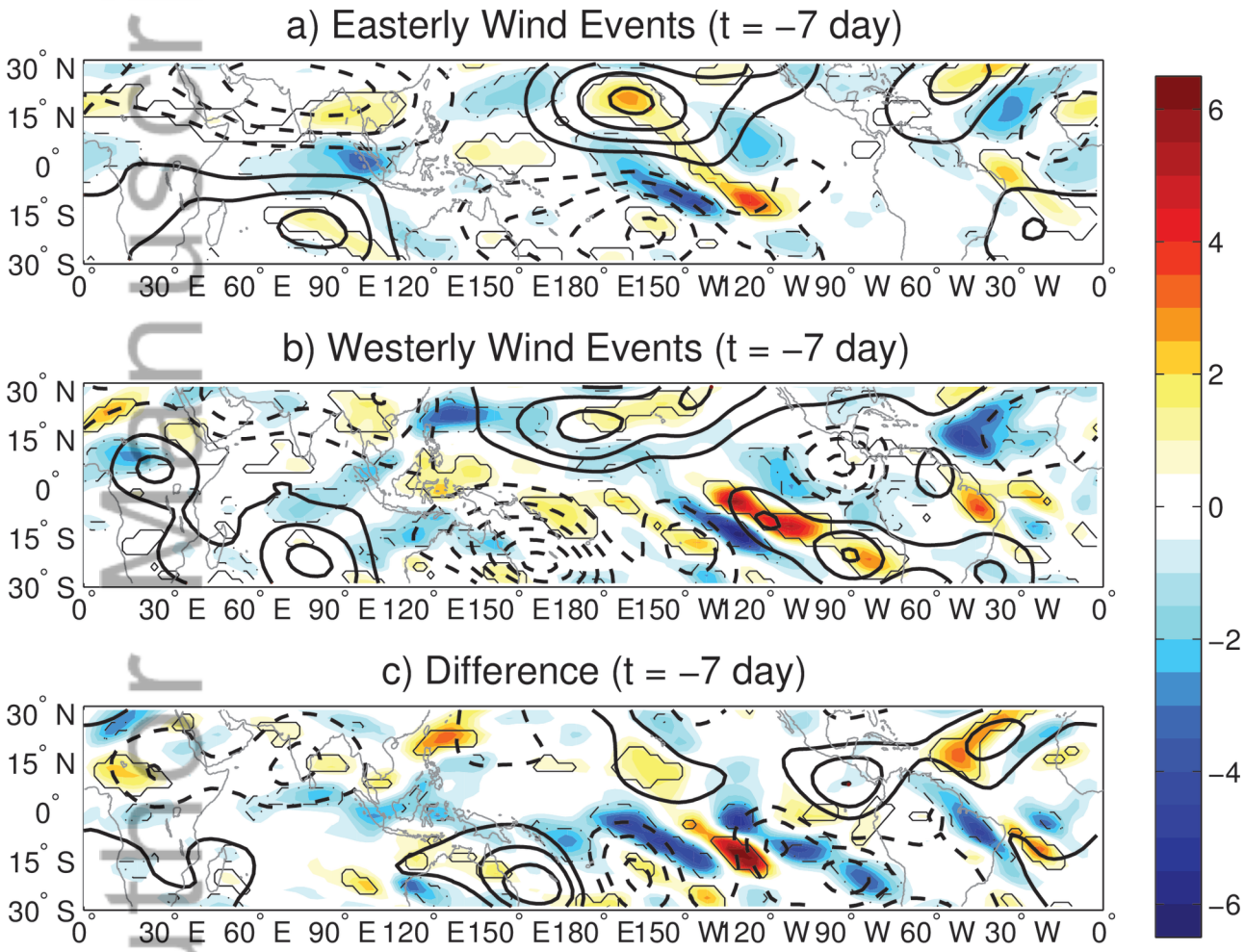

fig9_map_term3b_p125_t-7

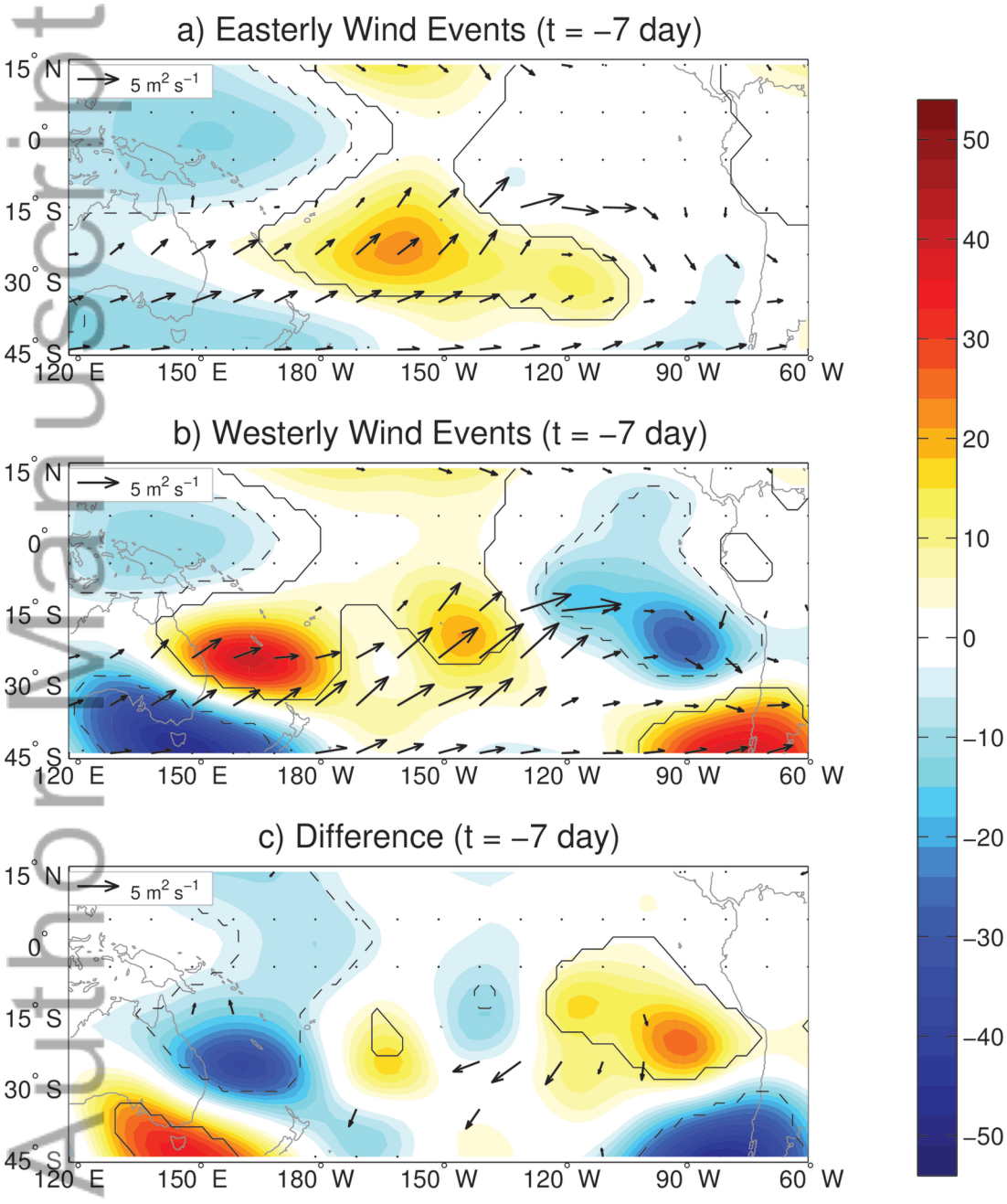

fig10_map_waveflux_p125_t-7

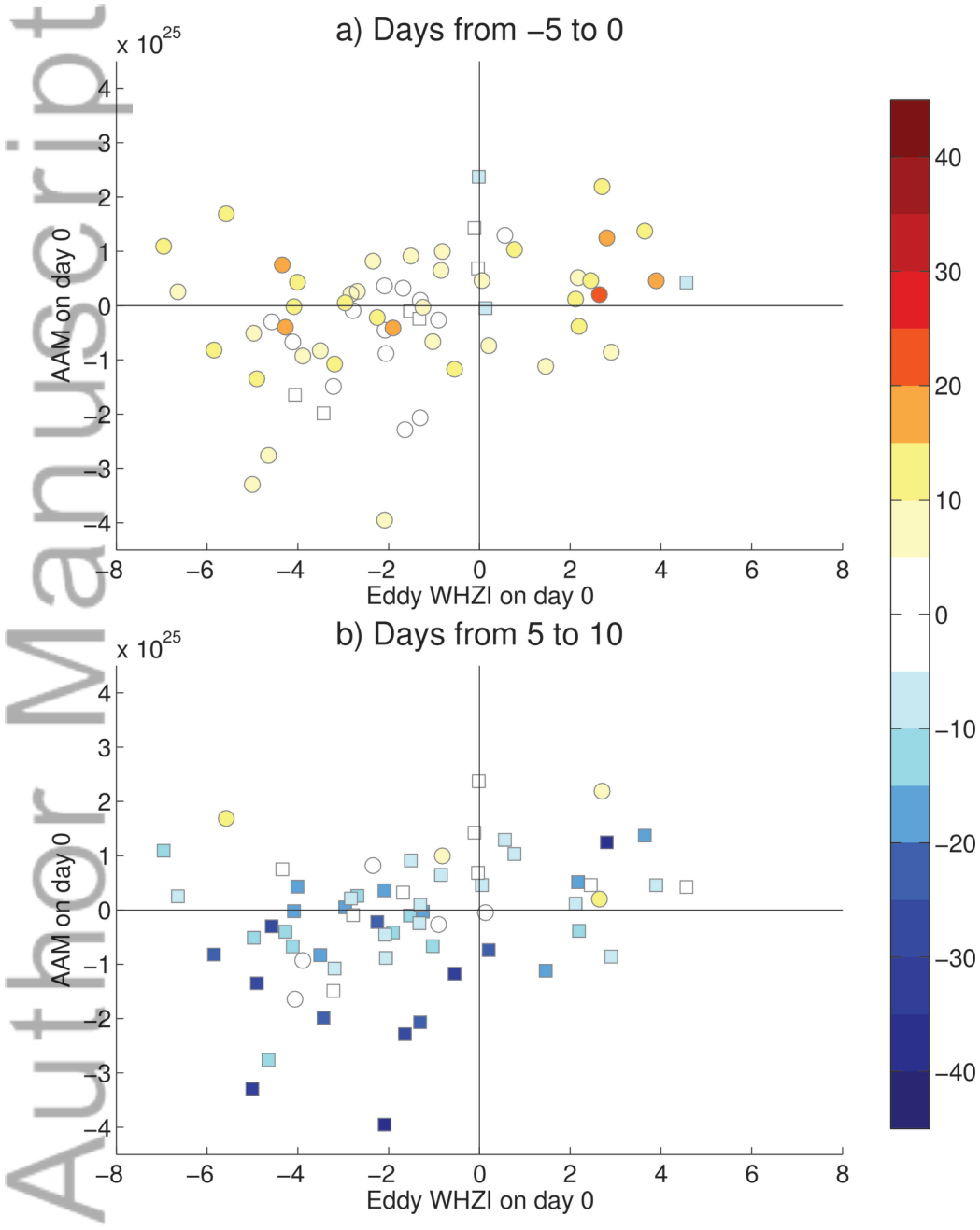

fig11_scatter_olrbase10n10s75e115e_whzieddy

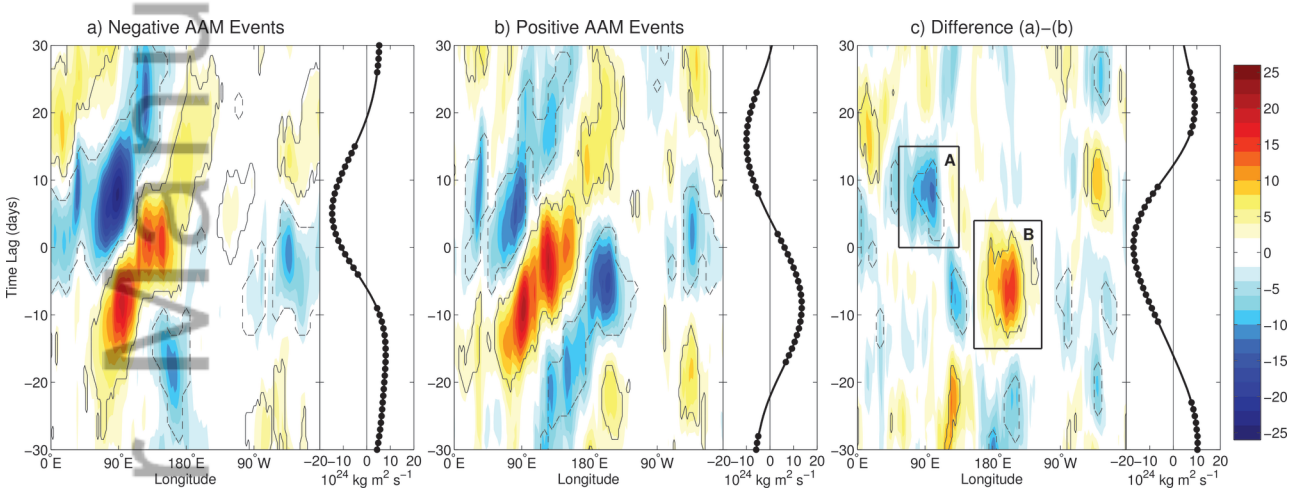

fig12_hovlon_olrmjoaameasterly_whzi

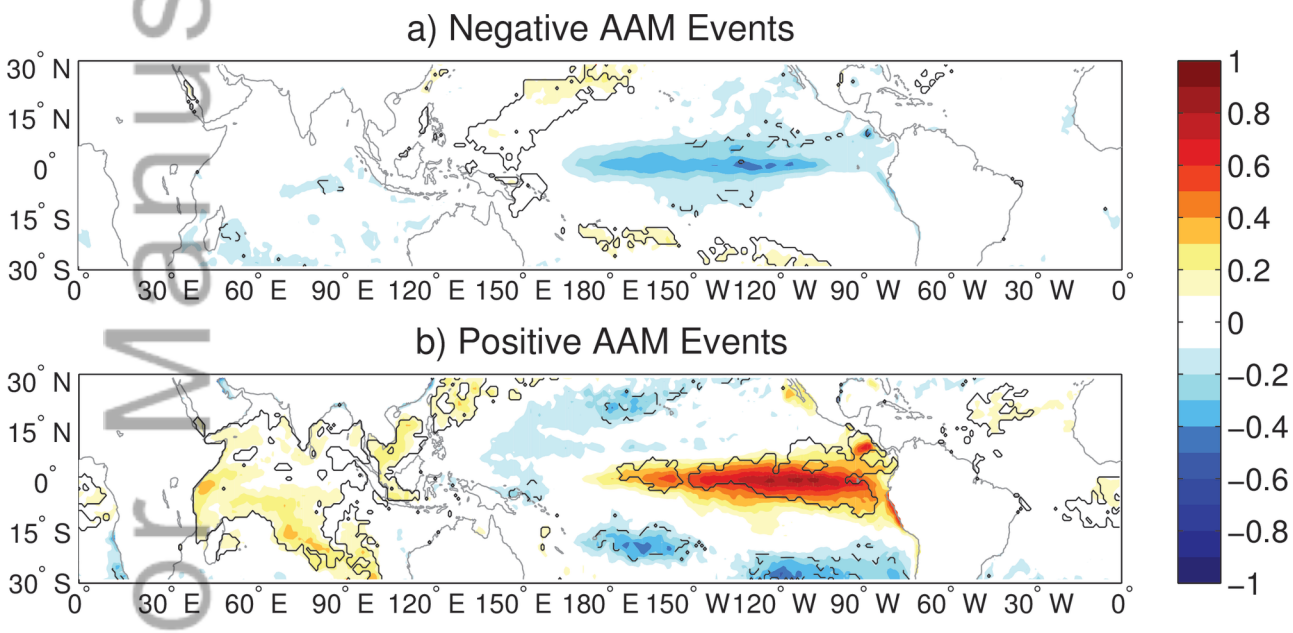

fig13_map_sstbar

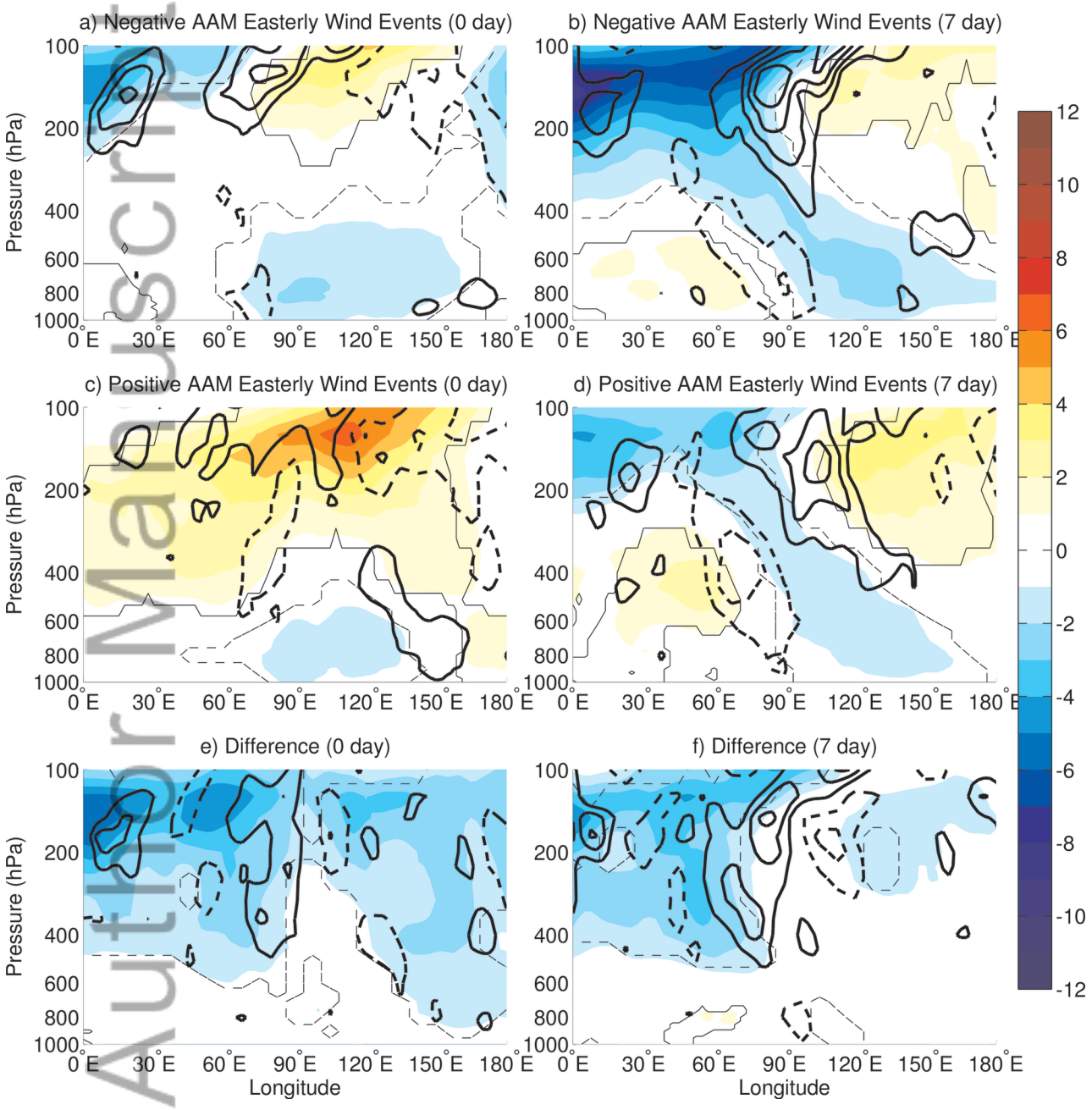

fig14_zonalxs_umjodumjodx_whzieddy_eaameuwh-waameuwh